17. A. Atkinson *et al.*, *Nat. Mater.* **3**, 17–27 (2004).
18. P. Moghimpour Bijani, M. Sohrabi, S. Sahebdelfar, *Chem. Eng. Technol.* **35**, 1825–1832 (2012).
19. Z. Cao *et al.*, *Angew. Chem. Int. Ed.* **52**, 13794–13797 (2013).
20. S. Liu, R. Ohnishi, M. Ichikawa, *J. Catal.* **220**, 57–65 (2003).
21. Chemical process simulation and optimization were performed using ASPEN PLUS v8.0 software.
22. Y. Shudo, T. Ohkubo, Y. Hideshima, T. Akiyama, *Int. J. Hydrogen Energy* **34**, 4500–4508 (2009).
23. National Energy Technology Laboratory, "Analysis of natural gas-to liquid transportation fuels via Fischer-Tropsch" (U.S. Department of Energy, DOE/NETL-2013/1597, 2013).

ACKNOWLEDGMENTS

This work was supported by the Research Council of Norway (grants 195912, 210418, 210765, and 219194) and the Spanish government (grants SEV-2012-0267 and ENE2014-57651). We thank the ALBA Synchrotron Light Laboratory for beam time provision. C.K. and P.K.V. have applied for a patent based on this work (PCT/EP2014/071697). Experimental data are available online at ftp://itqrepositorio.itq.upv.es/pub/.

SUPPLEMENTARY MATERIALS

www.sciencemag.org/content/353/6299/563/suppl/DC1
Materials and Methods
Figs. S1 to S9
Tables S1 and S2
References (*24*–*27*)

12 May 2016; accepted 12 July 2016
10.1126/science.aag0274

ANALYTICAL METHODS

Origin and hysteresis of lithium compositional spatiodynamics within battery primary particles

Jongwoo Lim,[1,2]* Yiyang Li,[1]* Daan Hein Alsem,[3] Hongyun So,[4] Sang Chul Lee,[1] Peng Bai,[5] Daniel A. Cogswell,[5] Xuzhao Liu,[1] Norman Jin,[1] Young-sang Yu,[6] Norman J. Salmon,[3] David A. Shapiro,[6] Martin Z. Bazant,[1,5,7,8] Tolek Tyliszczak,[6] William C. Chueh[1,2]†

The kinetics and uniformity of ion insertion reactions at the solid-liquid interface govern the rate capability and lifetime, respectively, of electrochemical devices such as Li-ion batteries. Using an operando x-ray microscopy platform that maps the dynamics of the Li composition and insertion rate in Li_xFePO_4, we found that nanoscale spatial variations in rate and in composition control the lithiation pathway at the subparticle length scale. Specifically, spatial variations in the insertion rate constant lead to the formation of nonuniform domains, and the composition dependence of the rate constant amplifies nonuniformities during delithiation but suppresses them during lithiation, and moreover stabilizes the solid solution during lithiation. This coupling of lithium composition and surface reaction rates controls the kinetics and uniformity during electrochemical ion insertion.

The insertion of a guest ion into the host crystal is the fundamental reaction underpinning insertion electrochemistry and has been applied to store energy (*1*), tune catalysts (*2*), and switch optoelectronic properties (*3*). In Li-ion batteries, for example, Li ions from the liquid electrolyte insert into solid host particles in the electrode. Nanoscale intraparticle electrochemical inhomogeneities in phase and in composition are responsible for mechanical strain and fracture, which decrease the reversibility of the reaction (*4*). Moreover, these nonuniformities make it difficult to correlate current-voltage measurements to microscopic ion insertion mechanisms. Simultaneously quantifying nonuniform nanoscale reaction kinetics and the underlying material composition at the solid-liquid interface holds the key to improving device performance.

A model material for investigating ion insertion reactions is Li_xFePO_4 ($0 < x < 1$), which separates into two phases at equilibrium (*5*). Recent studies using in situ x-ray diffraction revealed a continuous distribution of lattice constants at high rates of (de)lithiation (*6*–*9*). This finding supports the hypothesis that phase separation is suppressed during (de)lithiation and is replaced by a solid-solution crystallographic insertion pathway (*10*), consistent with theoretical predictions (*11*, *12*). Precise quantification of the Li composition (x) is difficult because the change in lattice constant convolves information from both Li composition and mechanical strain (*8*). Whereas heterogeneous current distributions between particles have been studied (*7*, *13*, *14*), there exists little understanding of how compositional nonuniformities evolve within individual particles. Diffuse interfaces have been proposed from diffraction patterns (*7*), but it is unclear where they occur or how they develop over time. Even less understood is the effect of interfacial reactivity on the single-particle lithiation pathway, which has been explored using models (*11*, *15*) but has not been probed experimentally.

In Li_xFePO_4, an insertion reaction changes x as well as the valence of Fe (*13*). Thus, tracking the spatial and temporal evolution of the Fe oxidation state reveals both the composition and the nanoscale insertion rate. Scanning electrochemical microscopy provides quantitative current-voltage measurement but is insensitive to the Li composition (*16*). Redox-sensitive liquid microscopy techniques such as transmission hard x-ray microscopy (*17*–*19*), fluorescence soft x-ray microscopy (*20*), and transmission electron microscopy (TEM) (*21*) have been used to track Li transport with single-particle sensitivity (*7*, *20*, *21*), or within agglomerates (*17*, *19*) in insertion electrodes. However, tracking the spatial evolution of lithiation within the same particles under multiple electrochemical conditions in liquid has not been realized because of insufficient spatial and temporal resolution, beam-induced damage, and/or low absorption contrast. Additionally, although three-dimensional x-ray microscopies have revealed important insights on the morphology, strain, and dislocation of single particles (*22*–*24*), quantitative measurement of the local insertion rate remains elusive.

We developed synchrotron-based liquid scanning transmission x-ray microscopy (STXM) to probe the spatiotemporal evolution of the Li composition and insertion rate within primary particles (Fig. 1A). Using a microfluidic electrochemical cell, we imaged the Li composition of ~30 single-crystalline, carbon-coated Li_xFePO_4 particles (Fig. 1, B and C) as they delithiated (charged) and lithiated (discharged) in an organic liquid electrolyte. This platelet particle morphology has been used in fundamental studies of Li_xFePO_4 (*20*, *25*–*27*). The particles' [010] crystallographic axis, which is the fast Li diffusion direction (*28*), lies parallel to the soft x-ray beam. We used operando STXM to track the change in the Fe oxidation state that accompanies lithiation at the Advanced Light Source STXM beam line 11.0.2.2 and at 5.3.2.1 (*29*). By raster-scanning Li_xFePO_4 platelet particles (~1 μm wide and 150 nm thick, specific capacity ~150 mAh g^{-1}; figs. S1 to S3) with a 50-nm x-ray probe, we acquired the nanoscale x-ray absorption spectra at the Fe L_3 edge (Fig. 1D), from which the local Li composition (x) can be quantified (*13*). Spectral analysis confirmed that the composition of solid-solution and phase-separating Li_xFePO_4 could

[1]Department of Materials Science and Engineering, Stanford University, Stanford, CA 94305, USA. [2]Stanford Institute for Materials & Energy Sciences, SLAC National Accelerator Laboratory, Menlo Park, CA 94025, USA. [3]Hummingbird Scientific, Lacey, WA 98516, USA. [4]Department of Aeronautics and Astronautics, Stanford University, Stanford, CA 94305, USA. [5]Department of Chemical Engineering, Massachusetts Institute of Technology, Cambridge, MA 02139, USA. [6]Advanced Light Source, Lawrence Berkeley National Laboratory, Berkeley, CA 94720, USA. [7]Department of Mathematics, Massachusetts Institute of Technology, Cambridge, MA 02139, USA. [8]SUNCAT Interfacial Science and Catalysis, Stanford University, Stanford, CA 94305, USA. *These authors contributed equally to this work. **†Corresponding author. Email: wchueh@stanford.edu**

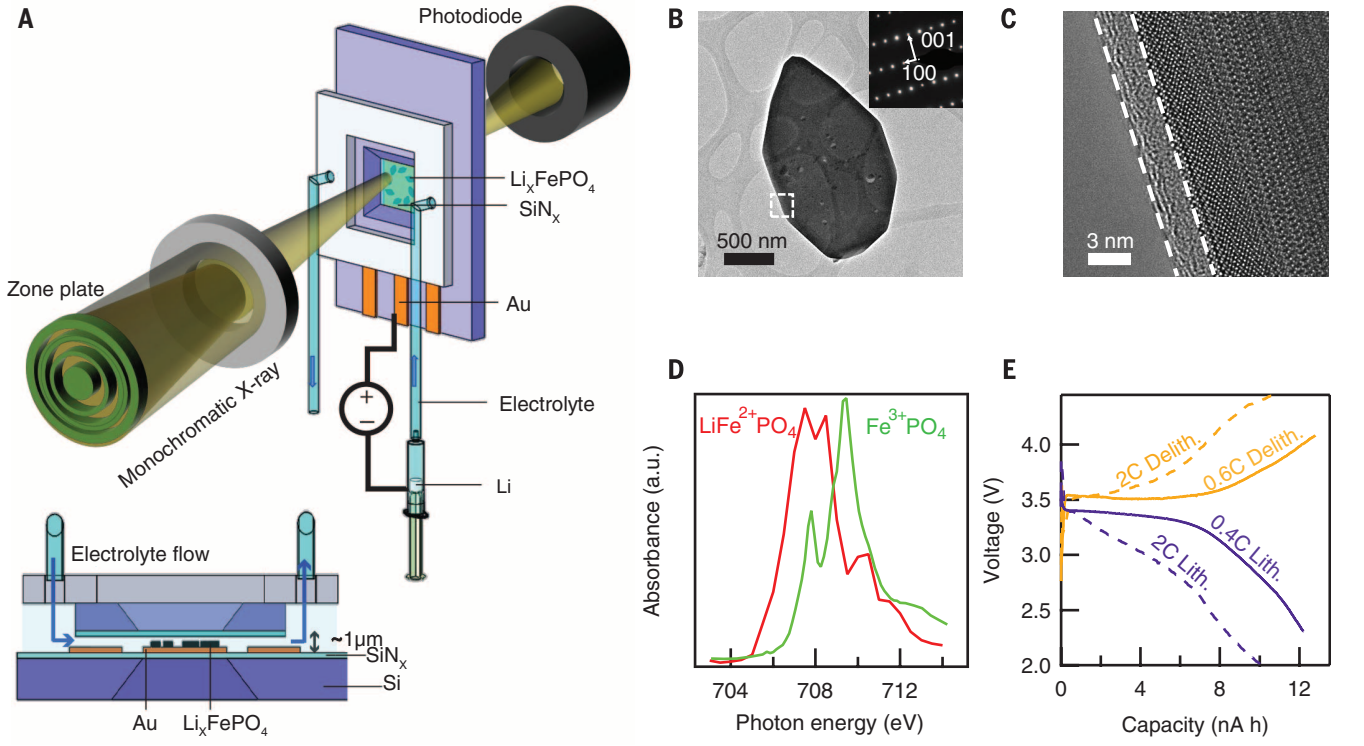

Fig. 1. Liquid STXM nanoimaging platform. (**A**) Schematic of the operando liquid imaging platform. The Li_xFePO_4/Au working electrode is placed in the sandwiched SiN_x stack, and the Li foil counter/reference electrode is placed in a syringe outside of the chamber, connected ionically via the electrolyte tube and electronically via a potentiostat. The inset shows a cross-sectional view of the cell. (**B**) Bright-field TEM and electron diffraction of a typical $LiFePO_4$ platelet particle. (**C**) High-resolution TEM of the carbon coating (outlined) of a $LiFePO_4$ particle. (**D**) Typical x-ray absorption spectra of $LiFePO_4$ and $FePO_4$ particles in liquid. (**E**) Electrochemical cycling of Li_xFePO_4 particles in the microfluidic liquid cell.

be determined through a linear combination fit of the end-member states (figs. S4 to S6), consistent with previous work (*13*, *20*, *30*).

In our setup, the battery particles are housed in a multimodal microfluidic electrochemical cell (Hummingbird Scientific), also used for liquid TEM (*21*, *31*). The liquid electrochemical cell consists of two sandwiched Si membrane chips, with 75-nm-thick SiN_x windows and fluoropolymer O-rings for imaging and sealing, respectively. The electrolyte (1.0 M $LiClO_4$ in tetraethylene glycol dimethyl ether) flows from the liquid inlet to the outlet, passing through the ~1-μm gap between the chips (Fig. 1A). The thin spacing minimizes attenuation of soft x-rays, and the flow of electrolyte minimizes interaction between the sample and the beam. The working electrode consists of a single layer of Li_xFePO_4 platelet particles dispersed on a 1.2 mm × 1.7 mm Au current collector (fig. S7), which was evaporated on one of the SiN_x membranes. By using a single layer of particles with an electrode porosity of >90%, we minimize tortuosity and transport losses at the electrode level. Low active material loading in this dilute electrode yields current density on the order of 0.1 μA cm^{-2} when normalized against the projected area of the current collector. This is approximately three orders of magnitude less than typical porous electrodes. Finite element analysis confirms that the electrolyte salt concentration and potential do not deviate from open-circuit values by more than 0.04 M and 2 mV, respectively, in the chip during cycling at 0.2C [where C indicates the rate to fully (de)lithiate the particles in 1 hour] and do not deviate by more than 0.2 M and 15 mV at 2C (fig. S8). The microfluidic cell has negligible capacitance or stray reactions (fig. S9) and uses a Li foil counter electrode (Fig. 1A). As a result, we observed the expected voltage plateau at ~3.4 V (Fig. 1E) and stable capacity (fig. S10) over multiple cycles, despite a low active material loading. At low rates, the electrochemical profile of the microfluidic cell was similar to that of a Li_xFePO_4 electrode cycled in a coin cell (fig. S3). At high rates, the profile deviated somewhat from that of coin cells. We hypothesize that these deviations arise from delamination of certain particles at higher rates; our analyses were conducted on particles that are not delaminated.

Figure 2A shows operando spectroimaging of a typical particle undergoing multiple delithiation and lithiation cycles. The particles successfully (de)lithiated electrochemically even after repeated exposure to the x-ray beam, reflecting the low x-ray dose (fig. S11) and high electrochemical fidelity. We tracked several particles (de)lithiating at 0.2C, 0.3C, 0.6C, and 2C (Fig. 2, A to C). The Li composition averaged over each particle (determined spectroscopically) corresponded to the mean composition of the electrode (determined electrochemically) (fig. S12). This implies that nearly all particles are active, consistent with previous reports on this particle morphology (*20*). We computed the single-particle C rate (Fig. 2, A to C) and confirmed that increasing the global current increases the rate of (de)lithiation of individual particles. When lithiated at a high rate of 2C, the operando Li composition maps (Fig. 2B and movie S1) show that the particles intercalated uniformly. In other words, there was little variation in composition across each particle, and the composition changed continuously over time from $x = 0$ to $x = 1$, as also quantified using line cuts (Fig. 3A). We interpret this as a solid-solution behavior. X-ray diffraction of the (020) reflection reveals strong diffraction intensity between the peaks for the Li-rich and the Li-poor phases, which suggests that phase separation along [010]—the direction parallel to the x-ray beam—is unlikely to explain the spatially uniform Li composition (fig. S13). This finding is consistent with the high elastic strain energy penalty of phase separation in that direction for our particle size (*15*, *32*).

We also conducted an ex situ experiment by mapping the Li composition in half-delithiated particles cycled at 1C and subsequently relaxed for ~12 hours (Fig. 2D). These particles displayed sharp phase boundaries between Li-rich and Li-poor regions. The phase boundaries follow the facets of the particle, consistent with an elastically driven process. The line cuts of x within a

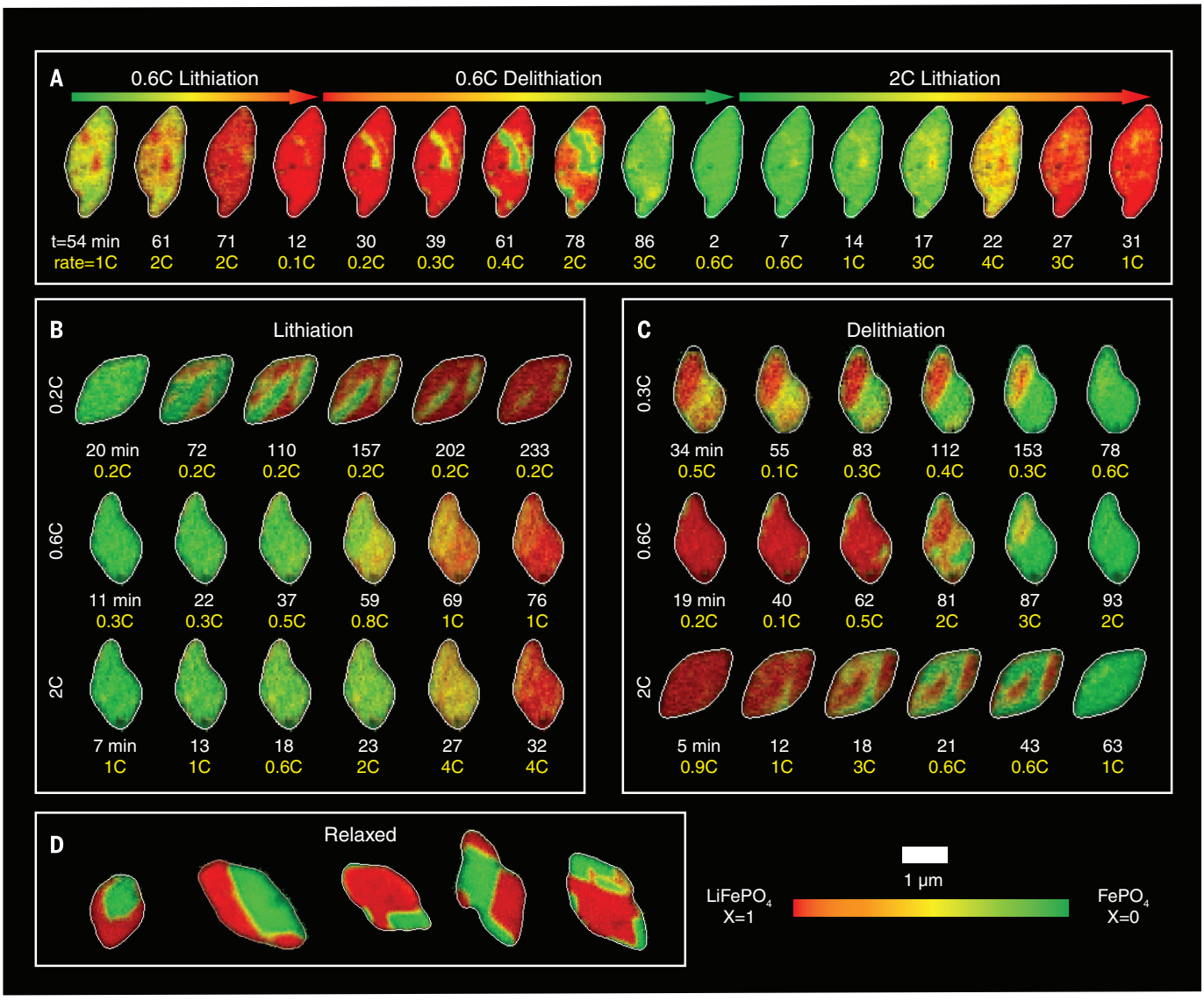

Fig. 2. Representative operando frames of Li insertion and extraction. (**A**) Operando Li composition frames of a single particle over multiple lithiation and delithiation cycles. The hue represents the Li composition (green, x = 0; red, x = 1). (**B** and **C**) Representative frames of different particles taken at various lithiation and delithiation rates, respectively. (**D**) Ex situ frames of Li composition for relaxed particles, showing the equilibrium distribution of Li within particles. Because the particle loading on the electrode is low, each acquired image typically contains a single particle, and this figure assembles multiple images together. Numbers below each frame indicate the time in minutes (white) and the C rate (yellow; see supplementary text for calculation protocol). t = 0 is defined as the starting time of the (de)lithiation cycle.

relaxed particle (Fig. 3B) clearly show that the Li composition is binary, where $x \approx 0$ or $x \approx 1$ for nearly every pixel. These observations, similar to previous ex situ studies (*25*, *26*) and theoretical calculations (*15*, *27*), confirm that phase separation under the influence of elastic strain dominates the equilibrium Li distribution.

A surprising observation for intermediate C rates (0.2C to 0.6C) during lithiation, and for all rates during delithiation, is that regions of fast Li ion (de)insertion and slow (de)insertion are visible (Fig. 2, B and C, and movie S2). Fast regions (de)lithiated preferentially while the remainder of the particle lagged behind. We term these regions "domains" because their Li composition is not binary, but rather varies continuously during cycling, as evident in the line cuts (Fig. 3A). This is a visualization of the compositionally nonuniform solid-solution pathway, where there exist many solid-solution domains in a single particle. At rates of 0.6C and higher, the electrochemical domains are largely circular or ellipsoidal, without being oriented with respect to the facets. At rates of 0.2C and 0.3C, the domain shapes contain both faceted and ellipsoidal features.

In contrast to standard phase-separation models that incorporate moving phase boundaries (*5*), intercalation waves (*33*), or domino cascades (*34*), we observed that the size of the fast domains (*35*) did not grow substantially in size. Rather, lithiation was accompanied by continuous change of the Li composition within each domain, with two or more concurrent solid-solution processes (Fig. 3C). Our results show that the presence of Li-rich and Li-poor regions within a single particle does not necessarily lead to moving phase boundaries. The slow growth of these domains can be explained because gradient energies, as modeled by Cahn-Hilliard–based reaction kinetics (*36*), slightly favor the (de)insertion of Li at domain boundaries (*11*).

We quantified the local current density within individual particles, calculated by evaluating the pixelwise difference in x between sequential frames (*35*). Because Li_xFePO_4 is a one-dimensional Li conductor (*28*), a change in x is attributed to ion insertion at the solid-liquid interface perpendicular to the ion conduction channels. Figure 3D maps the current density of several particles and shows domains of higher current density

relative to the rest of the particle. The same domains are fast under both lithiation and delithiation, thus confirming that the domain structures do not arise from random nucleation sites or spinodal decomposition. We rule out spatial variations in solid Li diffusion in the [010] direction as the origin of domain structures; the characteristic solid Li diffusion time in Li_xFePO_4 along the 150-nm-thick [010] direction is ~1 ms for x = 0 and ~10 ms for x = 1 (*28*), which are both much faster than total (de)lithiation times of 0.5 to 5 hours. We conclude that spatial variations in the insertion reaction kinetics at the solid-liquid interface give rise to these domain structures. The surfaces of the fast domains are more reactive for all Li compositions (fig. S16). We use "heterogeneity" to describe spatial variations in reaction rates, and "nonuniformity" to describe spatial variations in composition. Possible origins for these reaction heterogeneities include inhomogeneous strain (*24*), variations in carbon coating, and surface defects induced by cycling (*18*).

We quantified the degree of intraparticle composition uniformity by analyzing the standard deviation of x in each particle at every recorded frame (Fig. 3E and fig. S14). Our statistical analysis confirms that higher cycling rates reduce the variations in composition within a particle, resulting in more uniform intercalation (higher uniformity coefficient). Moreover, delithiation is substantially less uniform than lithiation. The statistical analysis and direct imaging of the same particle under different cycling rates show that Li_xFePO_4 exhibits (i) fully lithiated and delithiated regions (i.e., phase separation) when relaxed for an extended period of time, (ii) compositionally nonuniform solid solution (i.e., domains) at intermediate rates, and (iii) domain-free, compositionally uniform solid solution at high rates (summarized in Fig. 3F). In other words, the difference in the Li composition between Li-rich and Li-poor domains diminishes at higher rates of cycling, where the high applied overpotential stabilizes the uniform compositions for the same reasons that solid solution is stable with faster cycling (*6*, *8*, *9*, *11*, *15*). Consistent with this physical picture, restarting delithiation on a relaxed, phase-separated particle brings the particle into a solid solution, and a solid-solution particle phase separates over time when it is idle (fig. S15).

To understand the intrinsic ion insertion rate constant as a function of the Li composition, we identified a set of actively (de)intercalating pixels with approximately uniform composition in each particle at low cycling rates, and then spectroscopically measured the current density for that set of pixels. The chosen set of pixels lies within a single domain and intercalates uniformly. Because there is a disagreement regarding the quantitative relationship of current and overpotential between Butler-Volmer and Marcus kinetics (*37*), we limit our analysis to overpotentials of <120 mV. In this regime, the reaction models converge, and we used a linear relationship between current and voltage to extract the exchange current density (j_0) and quantify the reaction kinetics (*35*) (figs. S16 to S18).

By measuring the nanoscale j_0 at the subparticle level, our results show that the reaction rate depends strongly on x, the local Li composition (Fig. 4A): j_0 is low for Li-poor and Li-rich end members, likely because of low concentrations of Li ions and vacancies, respectively (*36*, *38*, *39*). We found that the magnitude of j_0 varies nonmonotonically with Li composition

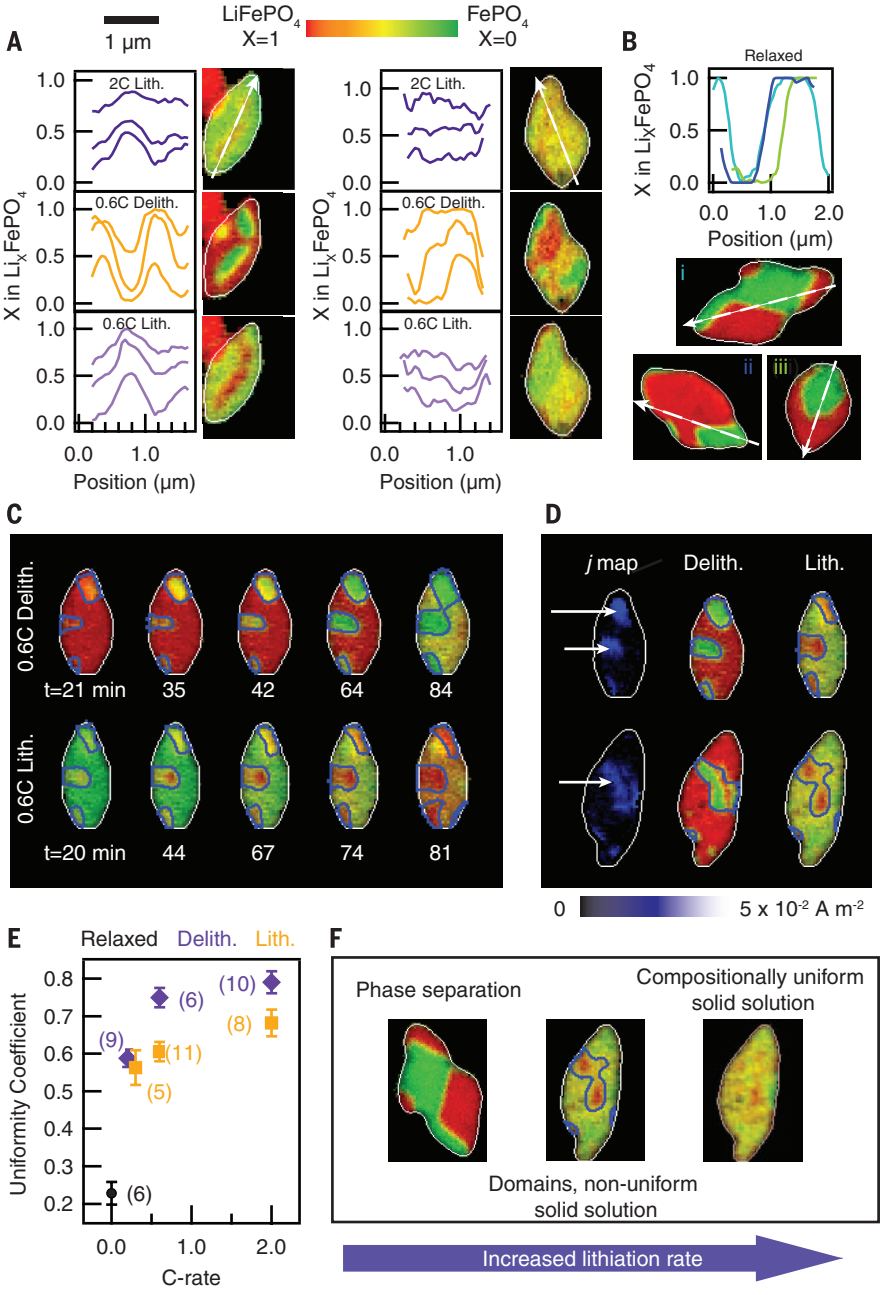

Fig. 3. Identification of domains in Li composition. (**A**) Line cuts of Li composition (x) of the same particles under different cycling conditions. The same pixels in a particle were sampled. (**B**) Line cuts of the relaxed, phase-separated particles. (**C**) The fast domains, outlined in blue, do not substantially grow in size. (**D**) Current density quantification reveals regions of higher insertion kinetics, calculated from delithiation. The same fast domains are present in both charge and discharge. (**E**) The uniformity coefficient increases with cycling rate and is consistently higher for lithiation than for delithiation. This was calculated from the standard deviation of x in each frame of a particle, where higher standard deviation indicates lower uniformity (see fig. S14). A coefficient of 0 indicates a binary distribution in the phase separation limit, whereas a coefficient of 1 indicates the uniform solid-solution limit. The value in parentheses indicates the number of particles analyzed under that condition. (**F**) Scheme of the insertion pathway as a function of the lithiation rate.

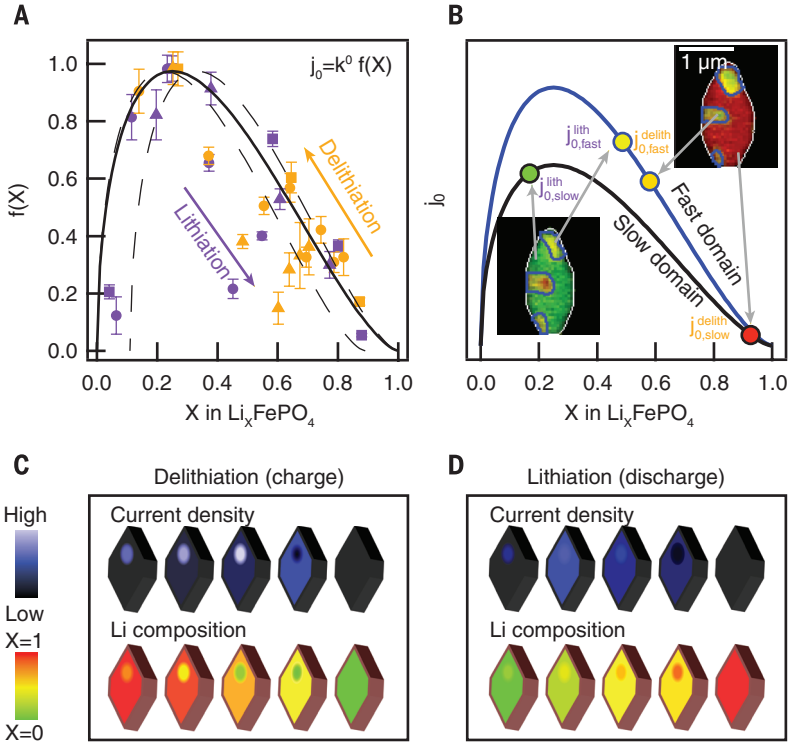

Fig. 4. Quantifying the insertion kinetics and exchange current density. (**A**) The measured exchange current density (j_0) varies nonmonotonically with the Li composition x. Solid line is a guide to the eye; k^0 is ~1 × 10^{-2} A m^{-2}. See supplementary text for error calculation. Each marker in each color represents a different particle. The dashed lines show the shifted j_0-x curve due to uncertainty arising from the fact that the specific capacity of the particles is less than the theoretical capacity. (**B**) Because the skewed j_0 peaks at $x \approx 0.25$, the value of j_0 for the fast domains is several times that of j_0 for the slow domains during delithiation, but the two quantities are comparable during lithiation. (**C**) During delithiation from $x = 1$ to $x = 0$, the fast domains have lower x, which amplifies the difference in current density between the two domains. (**D**) Upon lithiation from $x = 0$ to $x = 1$, the fast domains have higher x, reducing the difference in the current density.

and peaks at a composition of ~$Li_{0.25}FePO_4$. For the particles measured, j_0 peaks between 6×10^{-3} and 1×10^{-2} A m^{-2}. This composition-dependent j_0 reflects the defect chemistry of Li_xFePO_4 (*38*), whereby x modulates not only bulk thermodynamics and transport but also the surface kinetics of ion insertion. The skewed j_0-x relationship is in contrast to Newman's model (*39*), which is symmetric about $x = 0.5$. A skewed j_0-x curve was first proposed by Bazant using a general phase-field theory of chemical kinetics based on nonequilibrium thermodynamics (*36*). Following Bai, Cogswell, and Bazant (*11*, *15*), we conducted a linear stability analysis of the model and confirmed that such a skewed j_0-x curve is a necessary condition to suppress phase separation above a critical lithiation current (fig. S19). In contrast, the theory predicts that the solid-solution pathway is linearly unstable for a j_0 curve symmetric about $x = 0.5$ for all lithiation rates, although diffuse interfaces or quasi–solid solutions may still form.

The strong spatial and compositional dependence of j_0 within individual particles explains why domains persist more during delithiation than during lithiation. If the shape of the j_0-x curve is invariant between domains within a particle (fig. S16), the fast domains must consistently exhibit a higher j_0 for any x (Fig. 4B). During delithiation from $x = 1$, the rate accelerates from $x = 1$ to $x \approx 0.25$ (Fig. 4B). This positive feedback amplifies the difference in the reaction rate between slow and fast domains: The value of j_0 for the fast domain (which has a lower x) is much larger than for the slow domain (Fig. 4C). On the other hand, during lithiation from $x = 0$, the fast domain initially accelerates from $x = 0$ to $x \approx 0.25$ but decelerates once it passes $x \approx 0.25$, when j_0 starts to decrease with greater x. Because x is higher for the faster domain, this negative feedback diminishes the difference in reaction rate between the two domains (Fig. 4D). The acceleration regime during delithiation is larger than during lithiation by a factor of ~3 and quantitatively explains why delithiation is less uniform than lithiation. Thus, whereas high rates of lithiation yield nearly uniform compositions and current densities, similar rates of delithiation are highly nonuniform (Fig. 2C and Fig. 3, A and E). This skewed relationship may also describe some of the observed asymmetries in the voltage profile between charge and discharge. Other factors, such as an asymmetric charge transfer coefficient (*13*), may also contribute to the observed hysteresis.

Our results show that spatial heterogeneities in reaction rates account for the compositionally nonuniform solid-solution domains during (de)lithiation of Li_xFePO_4, and that the skewed j_0-x relationship amplifies reaction heterogeneities during delithiation but suppresses them during lithiation, consistent with theoretical predictions (*11*, *15*, *36*). These results highlight the crucial role of surface reaction rate in lithiation, with implications for electrode engineering and battery management. Higher rates of lithiation suppress compositional nonuniformities within particles and minimize mechanical stress, and have been shown to improve cyclability (*4*). However, the same statement is not true for delithiation, where reaction heterogeneities manifest as compositional nonuniformities. Beyond batteries, our work highlights the importance of composition in ion insertion kinetics, which affects a broad class of electrochemical materials.

REFERENCES AND NOTES

1. M. S. Whittingham, *Chem. Rev.* **114**, 11414–11443 (2014).
2. H. Wang *et al.*, *Proc. Natl. Acad. Sci. U.S.A.* **110**, 19701–19706 (2013).
3. A. Llordés, G. Garcia, J. Gazquez, D. J. Milliron, *Nature* **500**, 323–326 (2013).
4. W. H. Woodford, W. C. Carter, Y.-M. Chiang, *Energy Environ. Sci.* **5**, 8014–8024 (2012).
5. A. K. Padhi, K. S. Nanjundaswamy, J. B. Goodenough, *J. Electrochem. Soc.* **144**, 1188–1194 (1997).
6. X. Zhang *et al.*, *Nano Lett.* **14**, 2279–2285 (2014).
7. X. Zhang *et al.*, *Nat. Commun.* **6**, 8333 (2015).
8. H. Liu *et al.*, *Science* **344**, 1252817 (2014).
9. M. Hess, T. Sasaki, C. Villevieille, P. Novák, *Nat. Commun.* **6**, 8169 (2015).
10. J. Niu *et al.*, *Nano Lett.* **14**, 4005–4010 (2014).
11. P. Bai, D. A. Cogswell, M. Z. Bazant, *Nano Lett.* **11**, 4890–4896 (2011).
12. R. Malik, F. Zhou, G. Ceder, *Nat. Mater.* **10**, 587–590 (2011).
13. Y. Li *et al.*, *Nat. Mater.* **13**, 1149–1156 (2014).
14. W. Dreyer *et al.*, *Nat. Mater.* **9**, 448–453 (2010).
15. D. A. Cogswell, M. Z. Bazant, *ACS Nano* **6**, 2215–2225 (2012).
16. Y. Takahashi *et al.*, *Nat. Commun.* **5**, 5450 (2014).
17. J. Wang, Y. C. Chen-Wiegart, J. Wang, *Nat. Commun.* **5**, 4570 (2014).
18. Y.-S. Yu *et al.*, *Adv. Energy Mater.* **5**, 1402040 (2014).
19. J. Nelson Weker, Y. Li, R. Shanmugam, W. Lai, W. C. Chueh, *ChemElectroChem* **2**, 1576–1581 (2015).
20. Y. Li *et al.*, *Adv. Funct. Mater.* **25**, 3677–3687 (2015).
21. M. E. Holtz *et al.*, *Nano Lett.* **14**, 1453–1459 (2014).
22. M. Ebner, F. Marone, M. Stampanoni, V. Wood, *Science* **342**, 716–720 (2013).
23. J. N. Weker *et al.*, *Energy Environ. Sci.* **7**, 2771–2777 (2014).
24. A. Ulvestad *et al.*, *Science* **348**, 1344–1347 (2015).
25. D. A. Shapiro *et al.*, *Nat. Photonics* **8**, 765–769 (2014).
26. U. Boesenberg *et al.*, *Chem. Mater.* **25**, 1664–1672 (2013).
27. D. A. Cogswell, M. Z. Bazant, *Nano Lett.* **13**, 3036–3041 (2013).
28. D. Morgan, A. Van der Ven, G. Ceder, *Electrochem. Solid-State Lett.* **7**, A30–A32 (2004).
29. H. Bluhm *et al.*, *J. Electron Spectrosc. Relat. Phenom.* **150**, 86–104 (2006).
30. X. Liu *et al.*, *J. Am. Chem. Soc.* **134**, 13708–13715 (2012).
31. M. Gu *et al.*, *Nano Lett.* **13**, 6106–6112 (2013).
32. A. Abdellahi, O. Akyildiz, R. Malik, K. Thornton, G. Ceder, *J. Mater. Chem. A* **2**, 15437–15447 (2014).
33. G. K. Singh, G. Ceder, M. Z. Bazant, *Electrochim. Acta* **53**, 7599–7613 (2008).
34. C. Delmas, M. Maccario, L. Croguennec, F. Le Cras, F. Weill, *Nat. Mater.* **7**, 665–671 (2008).
35. See supplementary materials on *Science* Online.
36. M. Z. Bazant, *Acc. Chem. Res.* **46**, 1144–1160 (2013).
37. P. Bai, M. Z. Bazant, *Nat. Commun.* **5**, 3585 (2014).

38. J. Maier, R. Amin, *J. Electrochem. Soc.* **155**, A339–A344 (2008).
39. K. E. Thomas, R. M. Darling, J. Newman, *Advances in Lithium-Ion Batteries* (Kluwer Academic/Plenum, 2002).

ACKNOWLEDGMENTS

The x-ray component of this work was supported by the U.S. Department of Energy (DOE), Office of Basic Energy Sciences, Division of Materials Sciences and Engineering (contract DE-AC02-76SF00515). The battery component of this work was supported by the Ford-Stanford Alliance. The Advanced Light Source is supported by the DOE Office of Basic Energy Sciences under contract DE-AC02-05CH11231. N.J.S. and D.H.A. acknowledge support from the DOE Office of Basic Energy Sciences SBIR program under awards DE-SC-0007691 and DE-SC-0009573. Beam line 5.3.2.1 at the Advanced Light Source was funded through a donation by the King Abdullah University of Science and Technology. Also supported by a NSF Graduate Research Fellowship under grant DGE-114747 (Y.L.) and by the Global Climate and Energy Project at Stanford University and the DOE Office of Basic Energy Sciences through the SUNCAT Center for Interface Science and Catalysis (M.Z.B.). N.J.S. and D.H.A. are employed by Hummingbird Scientific, which designed and manufactured the microfluidic liquid cell used in these experiments. Part of this work was conducted the Stanford Nano Shared Facilities and the Stanford Nanofabrication Facility. We thank J. Nelson Weker, A. Wise, H. W. Shiu, M. Farmand, D. Kilcoyne, S. Fakra, Y. S. Hsieh, and A. Kammers for insightful discussions and assistance with the experiment.

The raw data for this experiment are available as part of the supplementary materials.

SUPPLEMENTARY MATERIALS

www.sciencemag.org/content/353/6299/566/suppl/DC1
Materials and Methods
Supplementary Text
Figs. S1 to S19
Movies S1 and S2
References (*40*–*49*)
Archive of Image Data

24 November 2015; accepted 8 July 2016
10.1126/science.aaf4914

NANOMATERIALS

Permanent excimer superstructures by supramolecular networking of metal quantum clusters

Beatriz Santiago-Gonzalez,[1]* Angelo Monguzzi,[1]*† Jon Mikel Azpiroz,[2,3] Mirko Prato,[4] Silvia Erratico,[5] Marcello Campione,[6] Roberto Lorenzi,[1] Jacopo Pedrini,[1] Carlo Santambrogio,[7] Yvan Torrente,[5] Filippo De Angelis,[2,4] Francesco Meinardi,[1]† Sergio Brovelli[1]†

Excimers are evanescent quasi-particles that typically form during collisional intermolecular interactions and exist exclusively for their excited-state lifetime. We exploited the distinctive structure of metal quantum clusters to fabricate permanent excimer-like colloidal superstructures made of ground-state noninteracting gold cores, held together by a network of hydrogen bonds between their capping ligands. This previously unknown aggregation state of matter, studied through spectroscopic experiments and ab initio calculations, conveys the photophysics of excimers into stable nanoparticles, which overcome the intrinsic limitation of excimers in single-particle applications—that is, their nearly zero formation probability in ultra-diluted solutions. In vitro experiments demonstrate the suitability of the superstructures as nonresonant intracellular probes and further reveal their ability to scavenge reactive oxygen species, which enhances their potential as anticytotoxic agents for biomedical applications.

Metal quantum clusters are functional nanoscale materials with potential for use in sensing (*1*), bio imaging (*2*), optoelectronics (*3*), and nanomedicine (*4*). With "magic" sizes dictated by the valence of the metal constituents (*5*) and dimensions approaching the Fermi wavelength of the electron, these few-atom structures bridge the gap between atoms and colloidal nanoparticles. As a result, metal quantum clusters combine a molecule-like electronic structure with quantum confinement effects that confer them with size- and shape-tunable optical properties, ultralarge surface-to-volume ratios, and unmatched flexibility for tailoring their physical properties through surface functionalization. Specifically, ligand-to-metal electron transfer (LM-ET) in metal quantum clusters with electron-rich capping agents (*6*–*8*) leads to strongly Stokes-shifted emission, which is beneficial for photon management (*9*) and bio imaging (*1*) applications. On the other hand, suppression of LM-ET results in intrinsic luminescence, with energy determined by the quantum mechanical combination of single-atom electronic orbitals (*10*, *11*). Fundamentally, the key common feature of "intrinsic emitting" metal quantum clusters is their capping with bulky molecules (*12*–*15*) or their encapsulation in supramolecular vesicles (*14*, *16*, *17*), imposing large distances between the metal cores. The use of short ligands, even in the absence of LM-ET, has led instead to a variety of optical behaviors (*18*–*21*). This points to a role of intercluster interactions in the photophysics of metal quantum clusters and suggests a supramolecular strategy for tuning their optical properties through controlled formation of aggregate species, similarly to what is achieved with organic chromophores.

In molecular physics, aggregate species are typically divided into two main categories based on the type of interaction that leads to their formation: Molecular dimers arise from ground-state interactions between individual moieties (monomers) (*22*), whereas excimers are evanescent quasi-particles existing exclusively in the excited state and formed through the aggregation of an excited monomer and a ground-state monomer. When excimers return to the ground state, their constituent monomers dissociate (*22*). As a result, dimers are capable of ground-state absorption, whereas excimers exhibit the absorption spectrum of the monomers and long-lived Stokes-shifted emission from lower-lying intermolecular states. Molecular excimers are typically formed through collisional interactions between monomers in concentrated solutions, and their formation probability drops to zero upon dilution (*23*). The excimer motif is, therefore, intrinsically prevented from being used for the fabrication of stable, self-standing emitters for single-particle applications.

In this work, we overcame this limitation by demonstrating a previously unknown aggregation state of matter that conveys the photophysics of excimers into individual particles that can find application as nonresonant emitters in cellular imaging and integrated photonic nanotechnologies. Specifically, we used Au_n (gold quantum clusters consisting of n atoms) as building blocks for fabricating permanent excimer-like colloidal superstructures (Au-pXs) held together by a network of hydrogen bonds between their capping ligands. As a result of repulsive forces between the metal cores, in the ground state, the networked Au_n behave as independent chromophores, whereas on photoexcitation, they form bimolecular excimers with largely Stokes-shifted emission (~1 eV). In contrast, encapsulation of Au_n in bulky vesicles hinders the excimeric interaction, resulting in the photophysics of isolated clusters. Last, we used Au-pXs for in vitro imaging

[1]Dipartimento di Scienza dei Materiali, Università degli Studi Milano-Bicocca, Via R. Cozzi 55, 20125 Milano, Italy. [2]Computational Laboratory for Hybrid and Organic Photovoltaics, National Research Council–Institute of Molecular Science and Technologies (CNR-ISTM), Via Elce di Sotto 8, 06123 Perugia, Italy. [3]Kimika Fakultatea, Euskal Herriko Unibertsitatea (UPV/EHU), and Donostia International Physics Center, 20080 Donostia, Euskadi, Spain. [4]Istituto Italiano di Tecnologia, Via Morego 30, 16163 Genova, Italy. [5]Dipartimento di Fisiopatologia Medico-Chirurgica e dei Trapianti, Università degli Studi di Milano, Fondazione IRCCS (Istituto di Ricovero e Cura a Carattere Scientifico) Cá Granda Ospedale Maggiore Policlinico, Centro Dino Ferrari, Via Francesco Sforza 35, 20122 Milano, Italy. [6]Dipartimento di Scienze dell'Ambiente e del Territorio e di Scienze della Terra, Università degli Studi Milano-Bicocca, Piazza della Scienza, 20125 Milano, Italy. [7]Dipartimento di Biotecnologie e Bioscienze, Università degli Studi Milano-Bicocca, Piazza della Scienza, 2 20126 Milano, Italy.
*These authors contributed equally to this work. †**Corresponding author. Email: angelo.monguzzi@mater.unimib.it (A.M.); meinardi@mater.unimib.it (F.M.); sergio.brovelli@unimib.it (S.B.)**

Science

Origin and hysteresis of lithium compositional spatiodynamics within battery primary particles

Jongwoo Lim, Yiyang Li, Daan Hein Alsem, Hongyun So, Sang Chul Lee, Peng Bai, Daniel A. Cogswell, Xuzhao Liu, Norman Jin, Young-sang Yu, Norman J. Salmon, David A. Shapiro, Martin Z. Bazant, Tolek Tyliszczak and William C. Chueh

Science **353** (6299), 566-571.
DOI: 10.1126/science.aaf4914

Watching batteries fail

Rechargeable batteries lose capacity in part because of physical changes in the electrodes caused by electrochemical cycling. Lim *et al.* track the reaction dynamics of an electrode material, $LiFePO_4$, by measuring the relative concentrations of Fe(II) and Fe(III) in it by means of high-resolution x-ray absorption spectrometry (see the Perspective by Schougaard). The exchange current density is then mapped for Li^+ insertion and removal. At fast cycling rates, solid solutions form as Li^+ is removed and inserted. However, at slow cycling rates, nanoscale phase separation occurs within battery particles, which eventually shortens battery life.

Science, this issue p. 566; see also p. 543

Science (print ISSN 0036-8075; online ISSN 1095-9203) is published by the American Association for the Advancement of Science, 1200 New York Avenue NW, Washington, DC 20005. The title *Science* is a registered trademark of AAAS.